


Systematic optical potentials for reactions with cluster-structured nuclei

L. Garrido-Gómez¹,* A. Vegas-Díaz¹, J. P. Fernández-García¹, and M. A. G. Alvarez¹
 Departamento FAMN, Universidad de Sevilla, Apartado 1065, 41080 Sevilla, Spain

 (Received 29 November 2023; revised 26 February 2024; accepted 22 April 2024; published 8 May 2024)

Background: Since 1919, when Rutherford measured the first nuclear reaction, and 1954, when Feshbach *et al.* [*Phys. Rev.* **96**, 448 (1954)] proposed the optical model (OM), as the simplest mathematical approach for describing nuclear reactions, a general description for stable, tightly and weakly bound, and exotic nuclei reactions is still missing. The Feshbach OM presents two advantages: (i) it converts a complicated problem of many bodies (nucleons) into a problem of two bodies (nuclei) through an average potential of interaction, and (ii) it proposes a complex (real and imaginary) mathematical description for the so-called optical potential (OP).

Purpose: We propose to study the OP (real and imaginary) strengths and their energy dependence, in reactions involving stable, tightly and weakly bound, and exotic nuclei projectiles on a ^{64}Zn target, at energies around the respective Coulomb barriers. We also propose to compare the current results to previous ones obtained for the same projectiles reacting on the heavier ^{120}Sn target.

Method: We analyze experimental elastic scattering angular distributions of ^4He , ^6Li , $^9,^{10},^{11}\text{Be}$, and ^8B impinging on the same (^{64}Zn) target, at bombarding energies around the respective Coulomb barriers. Within the data set, we report on OM calculations and the determined OP, with the respective uncertainties quantification, based on the double-folding (DF) São Paulo potential (SPP).

Results: Within the SPP approach, we compare the sensitivity of the OM theoretical predictions to different models assumed for the nuclear matter densities and to variations in the OP form factor and strengths. The best-fit parameters from OP study correlate with projectile breakup process, at scattering energies around the Coulomb barrier. Thus, we propose optimum energies for which the projectile breakup yield could be favored, as a function of the projectile breakup Q value and the Coulomb barrier of the system. The results are shown to be systematical, when analyzing different weakly bound nuclei projectiles impinging on targets with different masses (and atomic numbers). As a test of consistency, we apply the method to another specific case: $^7\text{Li} + ^{80}\text{Se}$.

Conclusion: The results represent important advances toward a fundamental mathematical description mainly for weakly bound nuclei reactions. The capability of predicting optimum projectile breakup yields, as a function of energy, represents an important tool for planning new experiments on weakly bound nuclei reactions. The determined OP must be of value for application to further calculations on such nuclei reactions, at energies around the Coulomb barrier, besides studying the OP dependence with energy.

DOI: [10.1103/PhysRevC.109.054608](https://doi.org/10.1103/PhysRevC.109.054608)

I. INTRODUCTION

The exact solution for a collision between heavy ions implies solving a many-body problem. Such a solution must take into account the interactions between all the nucleons in the projectile and each of the nucleons in the target. This fact makes any calculation extremely complex. Within this context, the optical model (OM) presents two fundamental characteristics to approach the problem: (i) the OM assumes the interaction between the projectile and the target through an average potential to represent the nucleon-nucleon interactions of the respective nuclei; (ii) this potential is complex: the real term represents the average potential in the nucleus, and the imaginary term represents the flux absorption from the elastic scattering to other reaction channels (such as inelastic

excitation, nucleon transfer, breakup, and/or fusion). The nuclear (real and imaginary) potential is then called the optical potential (OP) and is represented as a function of the distance between the interacting nuclei [1–3].

Elastic scattering is the simplest and most direct process involved in a nuclear reaction. It can be used as the starting point to understand more complicated reaction channels. For instance, it allows determining the OP, as input for more complex nuclear reactions calculations. From the last century through recent decades, different models have been used for the OP real and imaginary terms to reproduce a large number of elastic scattering data involving single nucleons to more complex heavy-ions systems, at a wide energy range [4–10].

Although far from being fundamental, OM analysis using the conventional Woods-Saxon (WS) form factor (with six free parameters), for the OP real and imaginary terms, has presented the best means for reproducing elastic scattering angular distributions [5]. However, there are problems

*Corresponding author: lgarrido2@us.es

in obtaining a simple model for systematizing the WS parameters, taking into account the nuclear densities, binding and bombarding energies dependence, refractive effects, etc. Particularly, for some systems, the variation with the bombarding energy requires arbitrarily different sets of OP parameters, with different form factors and strengths. This arbitrariness called for more realistic models for the OP.

It has been accomplished to a large extent by the double folding (DF) models, in general, and specifically by the DF nonlocal model, developed for the real term of the nucleus-nucleus interaction, coined the São Paulo potential (SPP) [11–15].

From OM analyses, it is known that the analysis of low-energy data, close to the Coulomb barrier, is sensitive to a surface region of the potential around the absorption radius [8]. Intermediate-energy data refer to refractive scattering, which is sensitive to a wider radial region [8,16]. The imaginary potential reflects, as a function of the energy, a large variety of physical effects: nuclear structure, channel couplings, reactions with various Q values, dispersion relation, etc. Polarization effects can affect both OP (real and imaginary) terms, and can be pronounced at energies around the Coulomb barrier. An extensive discussion on threshold anomalies and the dispersion relation is reported in [17]. In particular, different previous works [18,19] claimed anomalies in the OM analysis of weakly bound nuclei reactions, that could be related to the projectile breakup process. These so-called anomalies lead to renormalizing DF potentials in order to fit experimental data. In [20], the authors claimed a new manifestation of the dispersion relation, named the breakup threshold anomaly (BTA), which was further investigated and proposed by other works [21–24]. The main conclusion of these works is a decrease of the OP real strength accompanied by an increase of the OP imaginary ones, at energies around (even below) the Coulomb barrier. This effect is associated with a dynamic polarization potential due to the projectile breakup that could be important at a wide energy range.

Back to the DF SPP approach, in [25] a test of consistency was performed for its application to OM analyses. The same form factor was assumed for the OP real and imaginary terms, both based on the SPP, to describe reactions of stable tightly bound nuclei. Despite what one might expect, it was possible to obtain a reasonable data description, without applying free parameters. This fact is correlated to the greater sensitivity of the OM calculations to the real term of the interaction, which has been well accounted for by the SPP model. Therefore, the imaginary term was then obtained in a phenomenological way, through data fits, and did not provide a formal theoretical justification for its energy dependence. The results suggested the use of such a parameter-free model to get reasonable realistic estimations for heavy-ion elastic scattering and reaction cross sections. The extension of such findings to describe stable weakly bound and exotic nuclei reactions was then pursued [16,26,27].

In particular, several works were dedicated to describe exotic nuclei interactions using the SPP in OM analyses. For instance, in Ref. [28], the bare part of the OP was assumed by means of the SPP without any renormalization (even being applied to an exotic nuclei case: ${}^6\text{He}$). This bare interac-

tion was supplemented with a long-range Coulomb dipole polarization (CDP) potential, which takes into account the effect of the dipole Coulomb interaction. CDP was shown to increase the breakup probability and, therefore, to be crucial when analyzing exotic nuclei reactions. It was first verified with ${}^6\text{He}$, and it was corroborated by further analysis on ${}^{11}\text{Li}$ [29] and ${}^{11}\text{Be}$ [27]. This effect was deeply discussed in [29] and, more recently, in [27], in a more general analysis combining stable, tightly and weakly bound, and exotic nuclei reactions. CDCC calculations were able to distinguish the importance of Coulomb and/or nuclear effects, of different orders, for each specific nuclear reaction. Furthermore, CDCC calculations showed the importance of considering Coulomb and nuclear effects, of all orders, with the aim of describing the overall data trend.

In Ref. [26], a systematic study of reactions on the same ${}^{120}\text{Sn}$ target showed the SPP in the context of the standard strong surface absorption (SSA). The SPP, applied for the OP real and imaginary terms, provides a quite reasonable description of data for several projectiles. The set of projectiles also included stable, tightly and weakly bound, and exotic nuclei, at bombarding energies around the Coulomb barrier. The OM analyses resulted in an overall description with data even without allowing for free parameters. A better agreement is obtained when allowing the OP imaginary strength, responsible for taking into account elastic scattering flux absorption, to vary as a function of the bombarding energy.

In fact, within the SPP, as for other OP models, more accurate agreement between data and theoretical cross sections (data fit) can be obtained by considering adjustable parameters associated with the OP strengths. Notwithstanding, correlations between the OP real and imaginary strengths can lead to ambiguities and misunderstandings when interpreting such strengths [8].

In order to avoid the possible ambiguities inherent to OP real and imaginary strengths, the SPP for the OP real term used to be assumed with a fixed standard $N_r = 1$ factor, and only the imaginary strength of the OP is allowed to vary in the OM data fits. In Ref. [26], the same form factor was also applied to represent the OP (real and imaginary) strengths, based on the SPP. It was observed that the theoretical cross sections obtained through OM fits, with only one free parameter (N_i), are in quite good agreement with the data for all systems and energies [26]. Thus, the behavior of the best-fit OP imaginary strength has been studied and compared for several projectiles, in different energy regions. The OM analyses for weakly bound such as ${}^{10}\text{B}$, ${}^6,7\text{Li}$, and ${}^9\text{Be}$ projectiles resulted in significant OP imaginary strengths. This result indicates strong surface absorption, that can be extended even to low energies (below the Coulomb barrier). This is a characteristic related to the breakup (if not as the dominant process, at least as a competitive one) of weakly bound nuclei. It would be in agreement or consistent with previous reports [4,18–24]. Moreover, considering weakly bound nuclei, the increase of the OP imaginary strengths, at energies around the Coulomb barrier, is observed to follow an order: ${}^{10}\text{B}$, ${}^7\text{Li}$, ${}^6\text{Li}$, and ${}^9\text{Be}$. This order is related to the binding energy of these nuclei (see Table I). This can corroborate the breakup as the main (dominant) reaction process responsible for absorbing

TABLE I. Proton and neutron separation energies, cluster structure (possible mode of breakup), and corresponding Q value for the studied nuclei. All energies are provided in MeV. Data are extracted from [30].

Nucleus	S_p	S_n	Cluster	Q_{bu}
^4He	19.813	20.578		
^6He	22.59	1.710	$\alpha + n + n$	-0.975
^6Li	4.433	5.66	$\alpha + d$	-1.474
^7Li	9.973	7.251	$\alpha + t$	-2.468
^9Be	16.886	1.665	$\alpha + \alpha + n$	-1.665
^{10}Be	19.636	6.812	$^9\text{Be} + n$	-6.812
^{10}Be	19.636	6.812	$^6\text{He} + \alpha$	-7.409
^{11}Be	20.164	0.502	$^{10}\text{Be} + n$	-0.502
^8B	0.136	12.83	$^7\text{Be} + p$	-0.136
^{10}B	6.59	8.44	$^6\text{Li} + \alpha$	-4.461

flux from the elastic channel. Furthermore, from this analysis, this effect seems to be more prominent at a specific energy range, which correlates the projectile breakup Q value and the Coulomb barrier of the interacting system. For ^6Li and ^9Be , elastic scattering flux absorption is shown to be pronounced even below the Coulomb barrier, which should also be related to their lower binding energies and probability of breakup, that may compete with other reaction channels [4,18–24].

For further investigation in such a systematic OM study, the current paper analyzes the experimental elastic scattering angular distributions for several systems, with weakly bound nuclei projectiles impinging on another target (^{64}Zn), in a different region of mass [and atomic number (Z), changing from $Z = 50$ of ^{120}Sn to $Z = 30$ of ^{64}Zn]. Thus, we aim to cover three objectives: (i) to corroborate the previous result obtained for ^{120}Sn [26]; (ii) to demonstrate the target independence of such a result; and (iii) to demonstrate the systematic (projectile + target) OM analyses for weakly bound nuclei reactions. These three objectives determine the importance of including another target, in another region of mass/atomic number, in the OM analyses. It is worth mentioning the choice of ^{64}Zn is also related to the available data set in the literature. Predictions and data fits are proposed with the SPP assumed for different OM approaches.

In Sec. II, we present our optical model (OM) theoretical approaches. In Sec. III, we present the OM calculations and the respective comparisons with experimental data. In Sec. IV, we present further analysis and, finally, in Sec. V, we report a summary with our main conclusions and outlook.

II. THEORETICAL APPROACH

The new version of the São Paulo potential (SPP2), presented in Ref. [31], is based on a nucleon-nucleon interaction potential given by the following formula:

$$V_{\text{SPP2}}(r) = \iint U_0 \rho_1(\vec{r}_1) \rho_2(\vec{r}_2) e^{-(r/a)^2} e^{-4v^2/c^2} d\vec{r}_1 d\vec{r}_2. \quad (1)$$

Here, ρ_1 and ρ_2 are the projectile and target matter distributions, v is the relative velocity between projectile and target, c is the speed of light, $U_0 = -735.813$ MeV, and $a = 0.50$ fm.

In the present work, we propose the SPP2 theoretical approach [31] in the context of the OM to systematically study the elastic scattering data for the $^4,6\text{He}$ [32–34], $^6,7\text{Li}$ [35], $^9,10,11\text{Be}$ [36], and ^8B [37] systems, at energies around the Coulomb barrier, impinging on ^{64}Zn target.

For the sake of comparison, we perform OM calculations accounting only for the internal absorption from barrier penetration, based on the following OP approach:

$$U_N = V_{\text{SPP2}}(r) + iW(r), \quad (2)$$

where $W(r)$ is a Woods-Saxon type potential,

$$W(r) = W_0 / \{1 + \exp[(r - R_0)/a]\}, \quad (3)$$

with $W_0 = -100$ MeV, $R_0 = r_0(A_1^{1/3} + A_2^{1/3})$, $r_0 = 1.06$ fm, and $a = 0.25$ fm [26]. The small diffuseness simulates the fusion process and does not consider transitions to other peripheral nonelastic channels.

To describe the dynamics of the reactions, we use a complex nuclear potential given by

$$U_N = N_r V_{\text{SPP2}}(r) + iN_i V_{\text{SPP2}}(r). \quad (4)$$

N_r and N_i represent multiplicative factors that determine the strengths of the OP (real and imaginary) terms and simulate, in a simple form, the effects of the polarization potential. The polarization arises from nonelastic couplings. According to Feshbach's theory [1,2], it is energy dependent and complex. The imaginary term comes from transitions to open nonelastic channels that absorb flux from the elastic channel. The real term arises from virtual transitions to intermediate states (inelastic excitation and nucleon transfer, among others).

Elastic scattering angular distributions for many different nuclei have been successfully described using standard values $N_r = 1$ and $N_i = 0.78$ [25,26].

For the current systematic, we consider four OM approaches: the first one defined by Eq. (2); the second following Eq. (4) with the above standard parameters ($N_r = 1$ and $N_i = 0.78$) [25]; the third one following Eq. (4), allowing N_i to vary; and, finally, the fourth one following Eq. (4), allowing N_r and N_i to vary, in order to fit the experimental data set. These models will be referred to as OM1, OM2, OM3, and OM4 from now on.

With the aim of determining the uncertainties on OM3 and OM4 parameter(s), we assume the χ^2_{min} variation of χ^2_{min}/N , with N being the number of experimental data. The parameter uncertainty varies from the value with minimum χ^2 (χ^2_{min}) to the values with $(\chi^2_{\text{min}} + \chi^2_{\text{min}}/N)$. Thus, we assume the standard deviation to determine the confidence interval (1σ) of the fit parameter(s).

Table II–V compile the main results of OM1, OM2, OM3, and OM4 analyses with ^{64}Zn used as target. The best-fit OP parameter(s) with the respective uncertainties quantification, based on the above mentioned χ^2 analysis, are reported.

III. OPTICAL MODEL CALCULATIONS

The calculations and corresponding fits were performed using the FRESKO code and its routine SFRESKO [38]. The SPP2 was calculated with the REGINA code [31]. REGINA allows the

TABLE II. Results from OM3 best fits for ^4He , ^6Li + ^{64}Zn elastic scattering angular distributions, using theoretical and experimental nuclear densities. Energies are given in MeV.

Projectile	E_{CM}	χ_{theo}^2	χ_{exp}^2
^4He	12.42	2.64	0.86
	16.37	608	68
^6Li	10.77	1.29	1.40
	11.69	2.38	7.86
	12.43	6.22	22
	13.54	51	226
	14.92	97	322
	16.30	83	327
	18.14	42	296
	19.98	29	157

calculation of potentials based on experimental nuclear densities obtained from electron scattering experiments [39], or theoretical calculations obtained through the Dirac-Hartree-Bogoliubov (DHB) model [40].

A. OM sensitivity to the nuclear density models

Figure 1 presents nuclear matter densities for ^4He and ^6Li . Solid lines represent theoretical matter densities based on the DHB model. Dashed lines represent experimental densities obtained from electron scattering.

In Figs. 2(a) and 2(b), we are able to compare the sensitivity of the data fit to different models, for the ^4He nuclear

TABLE III. Results from OM2 fits. Energies are in MeV.

Projectile	V_{B}	E_{CM}	χ_{red}^2
^4He	9.4	12.42	1.44
		16.37	104
^6He	7.9	8.9	2.34
		12.4	11
		13.4	98
		16.2	381
		10.77	3.88
^6Li	12.6	11.69	3.69
		12.43	8.25
		13.54	53
		14.92	101
		16.30	134
		18.14	162
		19.98	75
		11.69	7.73
^7Li	12.4	12.43	74
		13.54	88
		14.92	168
		16.46	47
		18.14	50
^8B	21.1	34.22	2.17
^9Be	16.7	24.50	9.17
^{10}Be	16.6	24.50	13
^{11}Be	16.2	24.50	47

TABLE IV. Results from OM3 best fits. Energies are in MeV.

Projectile	V_{B}	E_{CM}	N_i	χ_{red}^2
^4He	9.4	12.42	0.61 ± 0.03	0.86
		16.37	0.43 ± 0.07	68
^6He	7.9	8.9	1.39 ± 0.38	2.11
		12.4	2.49 ± 0.38	3.50
		13.4	0.81 ± 0.26	98
		16.2	0.86 ± 0.21	380
^6Li	12.6	10.77	1.23 ± 0.07	1.29
		11.69	0.91 ± 0.04	2.38
		12.43	0.61 ± 0.06	6.22
		13.54	0.65 ± 0.13	51
		14.92	0.97 ± 0.22	97
		16.30	1.58 ± 0.31	83
		18.14	1.48 ± 0.11	42
		19.98	1.22 ± 0.09	29
^7Li	12.4	11.69	0.43 ± 0.04	2.30
		12.43	0.50 ± 0.12	56
		13.54	0.55 ± 0.17	82
		14.92	1.11 ± 0.26	154
		16.46	0.74 ± 0.17	47
		18.14	0.79 ± 0.14	50
^8B	21.1	34.22	1.01 ± 0.24	2.08
^9Be	16.7	24.50	0.67 ± 0.03	5.42
^{10}Be	16.6	24.50	1.41 ± 0.27	11
^{11}Be	16.2	24.50	7.5 ± 3.7	30

TABLE V. Results from OM4 best fits. Energies are in MeV; (*) indicates the absence of uncertainties is due to the insensitivity of the experimental data to OP parameters variation.

Projectile	E_{CM}	N_r	N_i	χ_{red}^2	
^4He	12.42	1.20 ± 0.11	0.83 ± 0.12	0.78	
	16.37	0.76 ± 0.03	0.32 ± 0.02	34	
^6He	8.9	0.38 ± 0.05	0.90 ± 0.15	0.24	
	12.4	0.55 ± 0.02	1.00 ± 0.06	0.39	
	13.4	0.25 ± 0.09	0.43 ± 0.03	66	
	16.2	0.17 ± 0.07	0.58 ± 0.02	196	
^6Li	10.77	1.05 ± 0.21	1.19 ± 0.16	1.29	
	11.69	0.60 ± 0.06	1.31 ± 0.06	0.69	
	12.43	0.58 ± 0.05	1.11 ± 0.06	0.92	
	13.54	0.66 ± 0.02	1.10 ± 0.04	1.05	
	14.92	0.64 ± 0.01	0.93 ± 0.02	1.15	
	16.30	0.67 ± 0.02	0.90 ± 0.03	2.10	
	18.14	0.75 ± 0.02	0.86 ± 0.04	2.34	
	19.98	0.73 ± 0.01	0.73 ± 0.02	1.19	
^7Li	11.69	0.61 ± 0.07	0.84 ± 0.07	0.78	
	12.43	0.62 ± 0.03	0.57 ± 0.04	1.24	
	13.54	0.66 ± 0.02	0.69 ± 0.02	0.84	
	14.92	0.63 ± 0.01	0.65 ± 0.01	0.72	
	16.46	0.59 ± 0.01	0.59 ± 0.01	1.06	
		18.14	0.64 ± 0.01	0.63 ± 0.01	0.68
^8B	34.22	0.30 ± 0.10	0.83 ± 0.06	0.96	
^9Be	24.50	1.08 ± 0.03	0.86 ± 0.07	3.59	
^{10}Be	24.50	1.28 ± 0.08	1.43 ± 0.05	8.52	
^{11}Be	24.50	0.09 (*)	8.63 (*)	30	

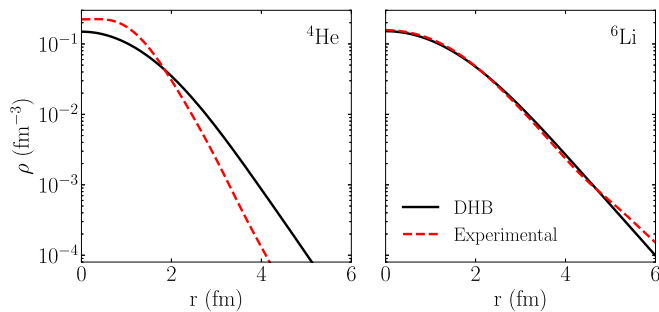


FIG. 1. Matter densities for ${}^4\text{He}$ and ${}^6\text{Li}$. Solid lines represent theoretical calculations obtained through the DHB model [40]. Dashed lines represent calculations [31] obtained from electron scattering experiments [39].

matter density, assumed in the DF approach. Figure 2(a) presents a reasonable agreement between data and the theoretical calculations, while Fig. 2(b) presents worse agreement. Reduced χ^2 (χ_{red}^2) values, obtained from OM3 fits, corroborate it (see Table II).

Figures 3 and 4 present results for ${}^6\text{Li} + {}^{64}\text{Zn}$, at energies ranging from $E_{\text{CM}} = 10.77$ MeV to $E_{\text{CM}} = 19.98$ MeV, for both experimental and theoretical projectile matter densities. The Coulomb barrier of this system is $V_B \approx 12.6$ MeV. Comparing Figs. 3 and 4, we verify that OM1 fails to fit the data. It is mainly accentuated in the rainbow (Coulomb-nuclear interference) region. Overall, OM2 and OM3 produce a reasonable agreement between them, and with data. Notwithstanding, applying the theoretical DHB model results in better data fits (see Fig. 4 and Table II). In Fig. 4, OM2 is shown to be slightly better to fit the rainbow region.

Therefore, nuclear densities represent a source of uncertainty in the folding type OP strength and respective OM analyses. Thus, any need to renormalize the OP real term,

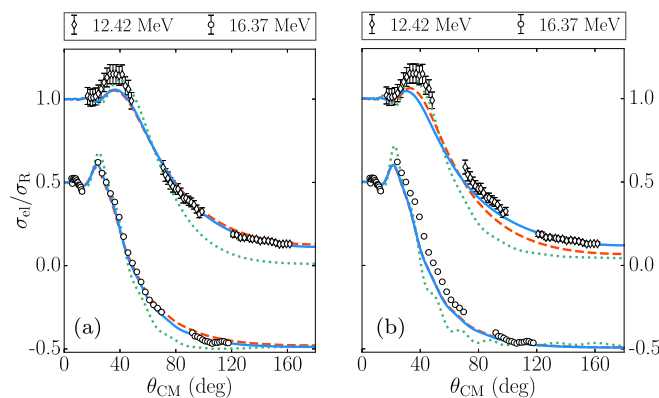


FIG. 2. Experimental elastic scattering angular distributions for the ${}^4\text{He} + {}^{64}\text{Zn}$ reaction. The Coulomb barrier is $V_B \approx 9.4$ MeV for this system. The dotted green line represents the theoretical cross section obtained with OM1, the dashed red line with OM2, and the solid blue line with OM3. For the sake of comparison, data for $E_{\text{CM}} = 16.37$ MeV have been shifted by a constant factor. Data were extracted from [33,34]. (a) Calculations using experimental nuclear densities and (b) Calculations using theoretical nuclear densities.

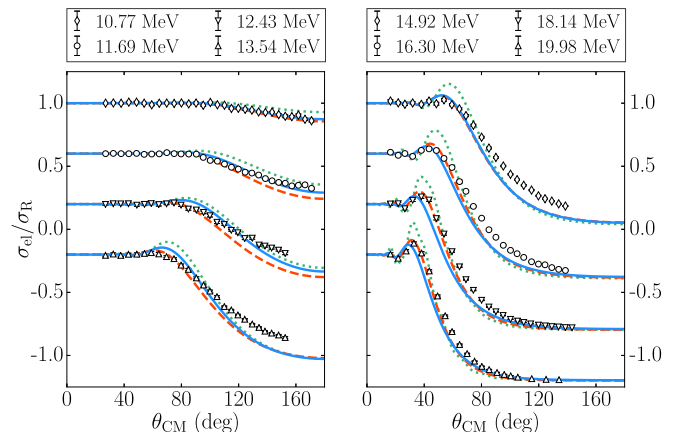


FIG. 3. Elastic scattering angular distributions for the ${}^6\text{Li} + {}^{64}\text{Zn}$ reaction. The Coulomb barrier is $V_B \approx 12.6$ MeV for this system. The experimental nuclear density of ${}^6\text{Li}$ was considered in the calculations. Data were extracted from [22]. See text for details.

within the data fit proposal could be, in the first instance, related to such uncertainty on nuclear densities models.

In next section, we present systematic OM calculations compared to experimental data. From now on, we assume the theoretical densities obtained through the DHB model, which is systematically applied in the SPP2 version of REGINA code [31].

B. OM theoretical calculations compared to experimental data

In Figs. 4–7, we compare data to theoretical calculations using OM1, OM2, and OM3, with the nuclear matter densities determined by the DHB model. The dotted green line represents the theoretical cross section obtained with OM1, the dashed red line with OM2, and the solid blue line with OM3. Tables III and IV present, respectively, OM2 and OM3 data fit results.

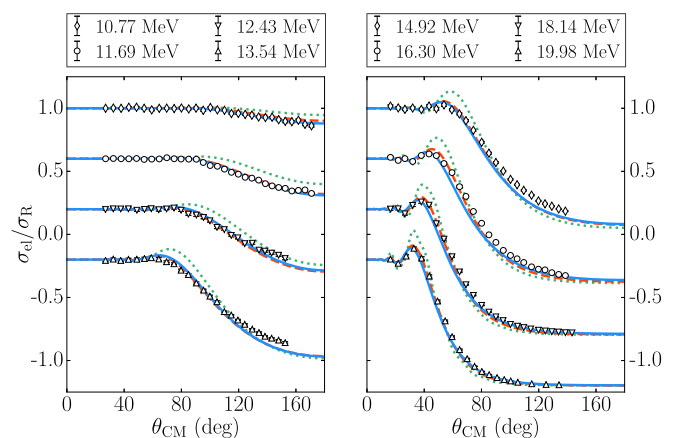


FIG. 4. Elastic scattering angular distributions for the ${}^6\text{Li} + {}^{64}\text{Zn}$ reaction. The Coulomb barrier is $V_B \approx 12.6$ MeV for this system. The theoretical DHB nuclear density of ${}^6\text{Li}$ was considered in the calculations. Data were extracted from [22]. See text for details.

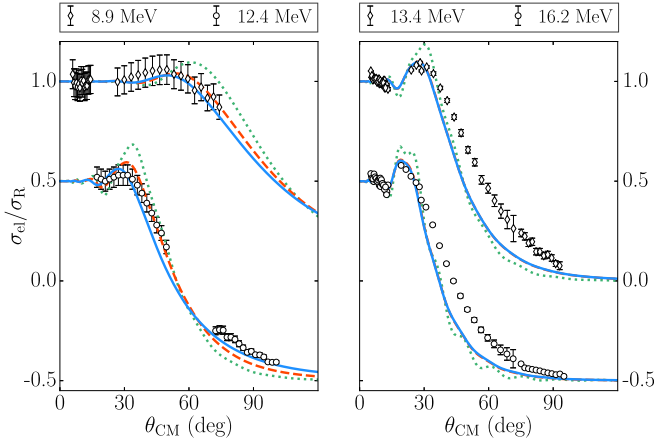


FIG. 5. Elastic scattering angular distributions for the ${}^6\text{He} + {}^{64}\text{Zn}$ reaction. The Coulomb barrier is $V_B \approx 7.9$ MeV for this system. Data were extracted from [34]. See text for details.

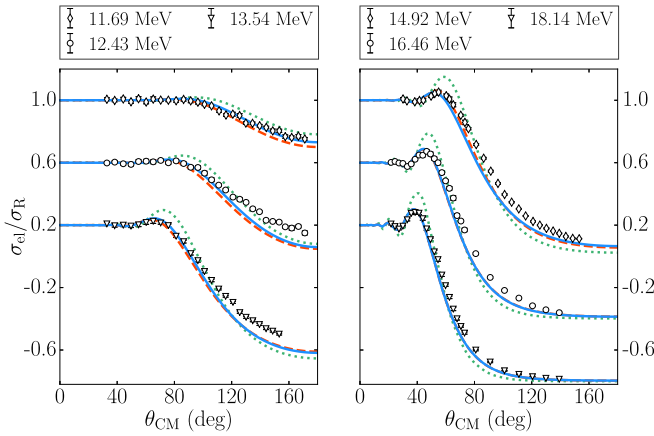


FIG. 6. Elastic scattering angular distributions for the ${}^7\text{Li} + {}^{64}\text{Zn}$ reaction. The Coulomb barrier is $V_B \approx 12.4$ MeV for this system. Data were extracted from [42]. See text for details.

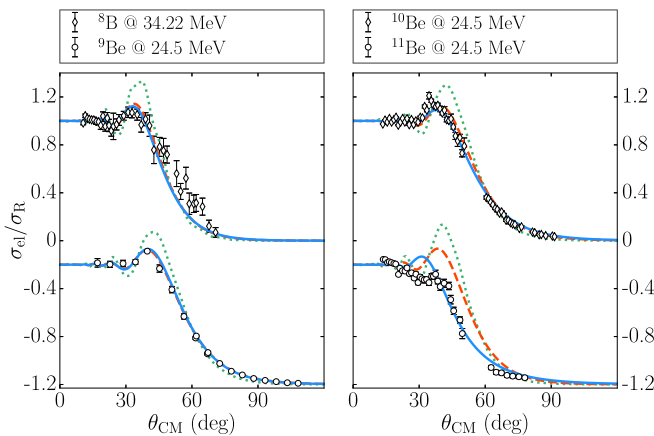


FIG. 7. Elastic scattering angular distributions for the ${}^8\text{B} + {}^{64}\text{Zn}$ and ${}^{9,10,11}\text{Be} + {}^{64}\text{Zn}$ reactions. The Coulomb barriers are $V_B \approx 21.1$, 16.7, 16.6, and 16.2 MeV, respectively, for these systems. Data were extracted from [37,43]. See text for details.

Figure 5 presents elastic scattering angular distributions for the reaction ${}^6\text{He} + {}^{64}\text{Zn}$, at energies ranging from $E_{\text{CM}} = 8.9$ MeV to $E_{\text{CM}} = 16.2$ MeV. The Coulomb barrier of this system is $V_B \approx 7.9$ MeV. OM1 fails fitting data, mainly considering the rainbow region. For lower energies, OM2 and OM3 present similar good agreement with data. OM2 fits data better at forward angles, while OM3 fits data better at backward angles. For higher energies, OM2 and OM3 fit data well at the rainbow region; however, fits at intermediate and backward angles have room for improvement. This mismatch can be improved by considering Coulomb and nuclear polarization effects [27,29,34].

Figure 6 presents results for ${}^7\text{Li} + {}^{64}\text{Zn}$, at energies ranging from $E_{\text{CM}} = 11.69$ MeV to $E_{\text{CM}} = 18.14$ MeV. The Coulomb barrier of this system is $V_B \approx 12.4$ MeV. As in the case of ${}^6\text{Li}$ (Figs. 3 and 4) and ${}^6\text{He}$ (Fig. 5) reactions, OM1 fails to fit data, which is mainly accentuated at the rainbow region. OM2 presents overestimated elastic scattering flux absorption, at backward angles and lower energies (closer to the Coulomb barrier). Overall, OM3 agrees better with the data by better accounting for such flux absorption. Small differences must be related to the uncertainties related to the nuclear matter density model and/or specific channel(s) that, once coupled, would provide a better data fit. For instance, in [41], the ${}^7\text{Li}$ elastic scattering angular distributions were shown to be strongly affected by couplings to the ${}^7\text{Li}$ first excited state [$E^* = 477.612(3)$ keV] [30].

Figure 7 presents results for ${}^8\text{B} + {}^{64}\text{Zn}$ and ${}^{9,10,11}\text{Be} + {}^{64}\text{Zn}$. The Coulomb barriers of these systems are, respectively, $V_B \approx 21.1$, 16.7, 16.6, and 16.2 MeV. Again, OM1 fails to fit data, which is even more accentuated in the rainbow region. OM2 and OM3 present a reasonable agreement with data for ${}^8\text{B}$ and ${}^{9,10}\text{Be} + {}^{64}\text{Zn}$. OM1 and OM2 fail to reproduce data of ${}^{11}\text{Be} + {}^{64}\text{Zn}$. The OM3 calculation presents a quite good agreement with ${}^{11}\text{Be} + {}^{64}\text{Zn}$ data, except for the rainbow region, where Coulomb and nuclear polarization effects play an important role [43].

Table IV presents the OM3 best fit N_i parameter with the respective uncertainty, as a function of the system and the bombarding energy. OM3 results for weakly bound nuclei reactions showed significant OP imaginary strength variations with energy, represented by the increase of the N_i parameter, that can persist even at sub-barrier energies.

In Table IV, the results of ${}^{10}\text{Be}$ and ${}^8\text{B}$ follow the trend, while the result of ${}^{11}\text{Be}$ shows a drastic pronounced increase in the OP imaginary strength. This result indicates a stronger surface absorption. It is a characteristic related to the breakup process of exotic weakly bound systems. The results are in agreement with previous studies reported in [26,27].

In order to better fit the data, we applied a fourth model, based on Eq. (4), allowing both parameters (N_r and N_i) to vary. The variation of the N_r parameter can allow for a more realistic OP, better description of elastic scattering angular distributions, and more precision when calculating nuclear reaction cross sections, besides putting some light on dynamic polarization effects, that can lead to the breakup threshold anomaly claimed in previous work [17–24,44,45] (see Sec. IV B).

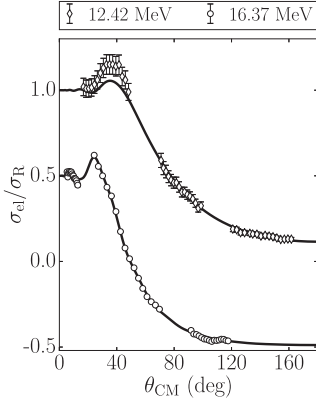


FIG. 8. Experimental elastic scattering angular distributions for the ${}^4\text{He} + {}^{64}\text{Zn}$ reaction and corresponding OM4 fits.

Table V presents the best fit (N_r , N_i) parameters, with the respective uncertainties. In addition, Table V presents the reduced χ^2 (χ_{red}^2), for each system, as a function of the bombarding energy.

Using Figs. 8–12 and Table V, we can compare the agreement between experimental data and the respective OM fit. Most χ_{red}^2 results are around the unity.

Using Tables. III to V, we are able to verify the continuous χ_{red}^2 improvement from OM2 to OM4.

The few exceptions are mainly related to variations in the rainbow structures. In particular, rainbow suppression is a common characteristic of exotic nuclei reactions. Such an effect is not accounted for by theoretical OM calculations, unless long range OP components are considered or continuum discretized coupled channel calculations (CDCC) are performed, in order to take breakup couplings into account [27,29].

In the specific case of ${}^{11}\text{Be}$, in Table V, a drastic variation in the OP real and imaginary strengths can be observed, with the worst χ_{red}^2 result. In this case, the absence of uncertainties is due to the insensitivity of the experimental data to OP parameters variation. In [43], Coulomb and nuclear couplings

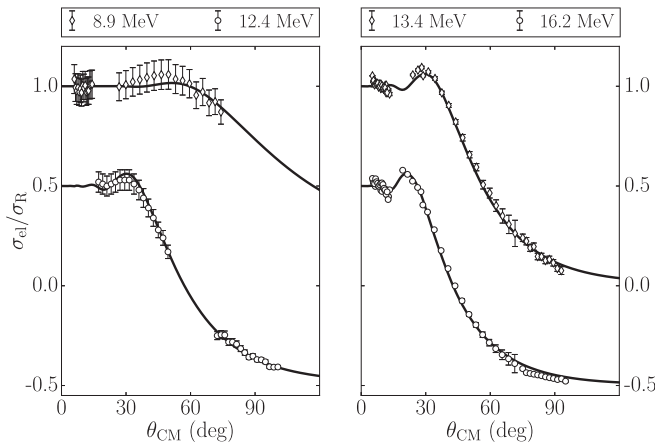


FIG. 9. Experimental elastic scattering angular distributions for the ${}^6\text{He} + {}^{64}\text{Zn}$ reaction and corresponding OM4 fits.

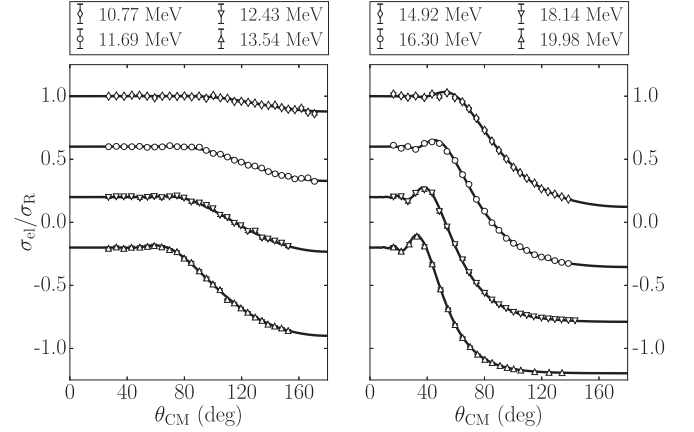


FIG. 10. Experimental elastic scattering angular distributions for the ${}^6\text{Li} + {}^{64}\text{Zn}$ reaction and corresponding OM4 fits.

to breakup channels were explicitly taken into account, by means of CDCC calculations, and their importance has been reported.

IV. ANALYSIS

We analyze experimental elastic scattering angular distributions of different projectiles (${}^4,6\text{He}$, ${}^6,7\text{Li}$, ${}^9,10,11\text{Be}$, and ${}^8\text{B}$) impinging on the same target (${}^{64}\text{Zn}$), at bombarding energies around the respective Coulomb barriers. Within the data set, we report on four different optical model (OM) analyses, based on the DF SPP approach, coined OM1, OM2, OM3, and OM4.

The OM1, with a different form factor compared to the others, is based on Eq. (2). OM1 takes into account internal fusion processes and does not take into account strong surface absorption (SSA) mechanisms. Thus, OM1 is range limited and fails when accounting for SSA.

OM2, based on Eq. (4), with fixed standard ($N_r = 1$ and $N_i = 0.78$ [25]) parameters accounts better for SSA. OM2 is confirmed to be a useful tool to obtain realistic nuclear reactions angular distributions.

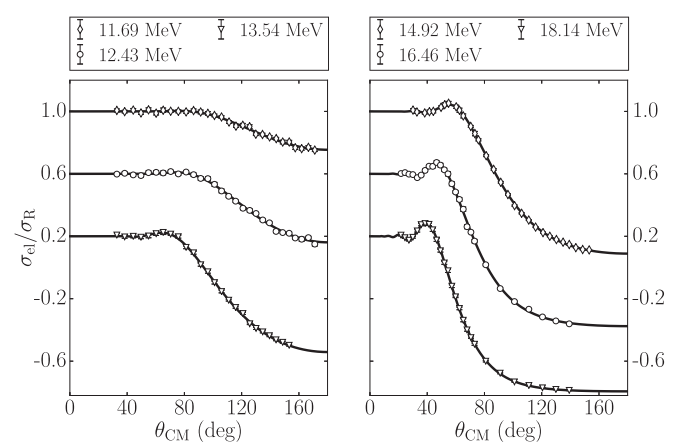


FIG. 11. Experimental elastic scattering angular distributions for the ${}^7\text{Li} + {}^{64}\text{Zn}$ reaction and corresponding OM4 fits.

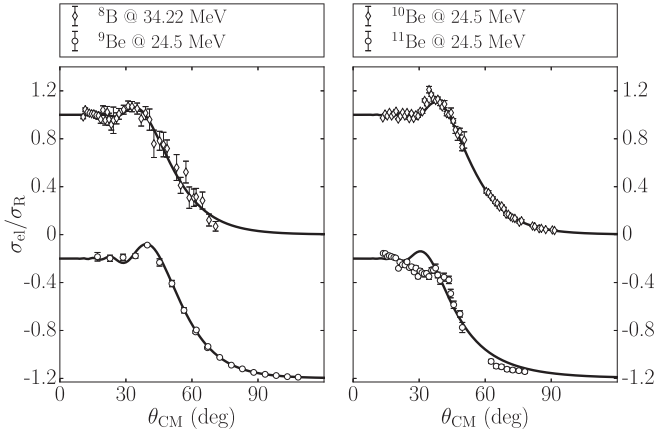


FIG. 12. Experimental elastic scattering angular distributions for the ${}^8\text{B} + {}^{64}\text{Zn}$ and ${}^{9,10,11}\text{Be} + {}^{64}\text{Zn}$ reactions and corresponding OM4 fits.

As a representative example for the OM2 application, Fig. 13 presents results obtained by fitting the ${}^9\text{Be} + {}^{64}\text{Zn}$ experimental elastic scattering angular distribution at $E_{\text{CM}} = 24.5$ MeV. Figure 13(a) presents χ^2 versus N_i for fixed N_r values. The best χ^2 values are obtained around $N_r = 1$. Figure 13(b) presents χ^2 in the N_i - N_r plane (heat map), in which the OM2 prediction results in the (hotter) region with better χ^2 values. Figure 13(c) presents optimal N_i as a function of

N_r and corresponding χ^2 . The best χ^2 values are obtained for $N_r = (1.08 \pm 0.03)$ and $N_i = (0.86 \pm 0.07)$. The OM2 analysis on, for instance, ${}^9\text{Be} + {}^{64}\text{Zn}$ at $E_{\text{CM}} = 24.5$ MeV, shows to be sensitive to χ^2 method with uncertainties on OP parameters ranging from 2% on N_r to 8% on N_i determination.

Despite the reasonable overall agreement provided by the OM2 model, it is limited to describing couplings to strong breakup channels, which are shown to be quite important for stable weakly bound and exotic nuclei reactions [27–29]. Such a limitation is stressed at determined energies, which seems to be related to the opening of specific cluster breakup channels presented in Table I.

As in the case of Ref. [26], in order to better take significant absorption process(es) into account, we consider OM3 for a systematic analysis.

The OM3 model is based on Eq. (4), where the SPP for the OP real term is assumed with the fixed standard $N_r = 1$ factor, and only the OP imaginary strength (by means of N_i factor) is allowed to vary, in the OM data fits. Thus, overall, OM3 agrees better with the data than OM2, once OM3 overcomes the OM2 limitation accounting for strong absorption (breakup) channels. See Tables III and IV for comparisons.

Figure 14 presents the N_i values as a function of the reduced energy, $E_{\text{red}} = E_{\text{CM}} - V_B$, for several projectiles reacting on two different targets, ${}^{64}\text{Zn}$ and ${}^{120}\text{Sn}$ (data extracted from [26]), respectively. The solid lines are only guides for the eye. The dashed horizontal line corresponds to the

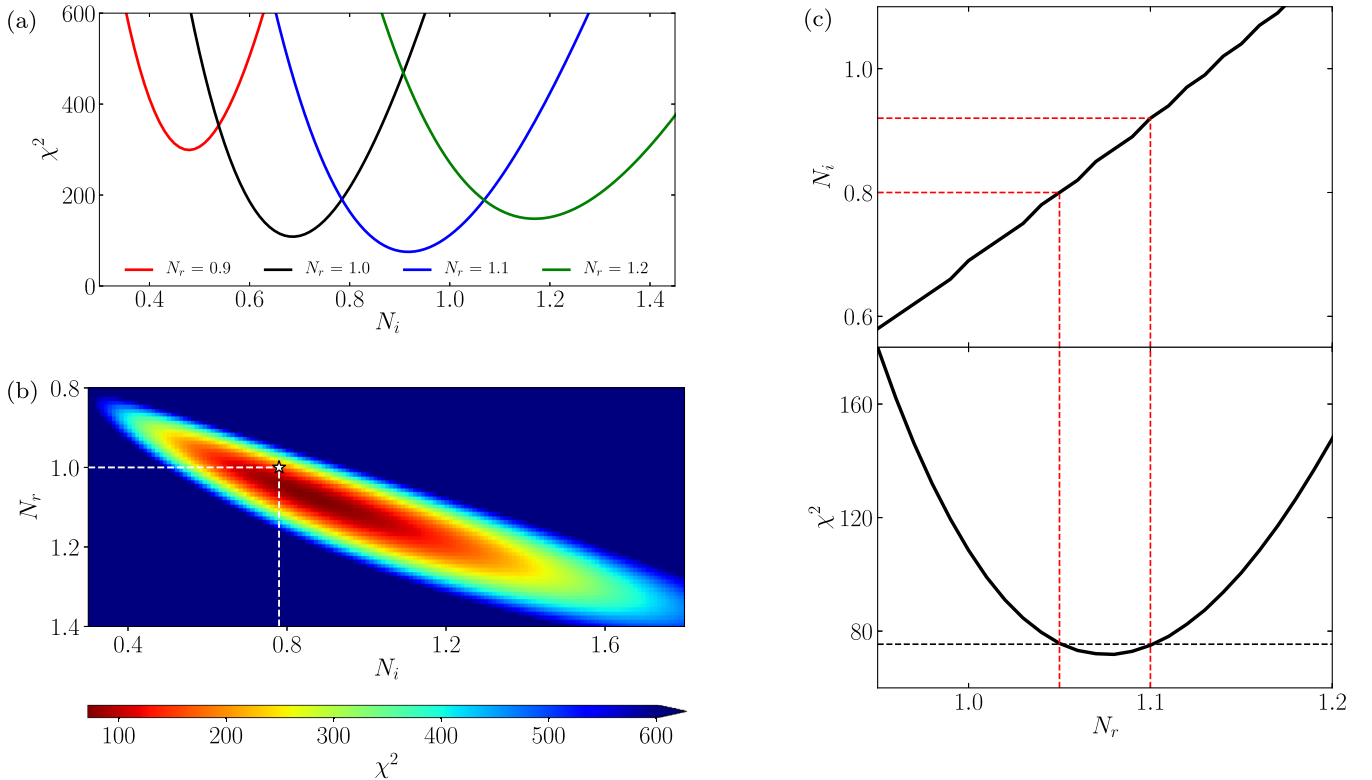


FIG. 13. χ^2 as a function of the fit parameters for the ${}^9\text{Be} + {}^{64}\text{Zn}$ fit at $E_{\text{CM}} = 24.5$ MeV. The figure also shows the correlation between N_r and N_i . The point $N_r = 1$, $N_i = 0.78$ (OP parameters that define OM2) is highlighted with a star. (a) χ^2 versus N_i for fixed N_r values. (b) χ^2 in the N_i - N_r plane. (c) Optimal N_i as a function of N_r and corresponding χ^2 . Parameter uncertainties are highlighted with dashed red lines.

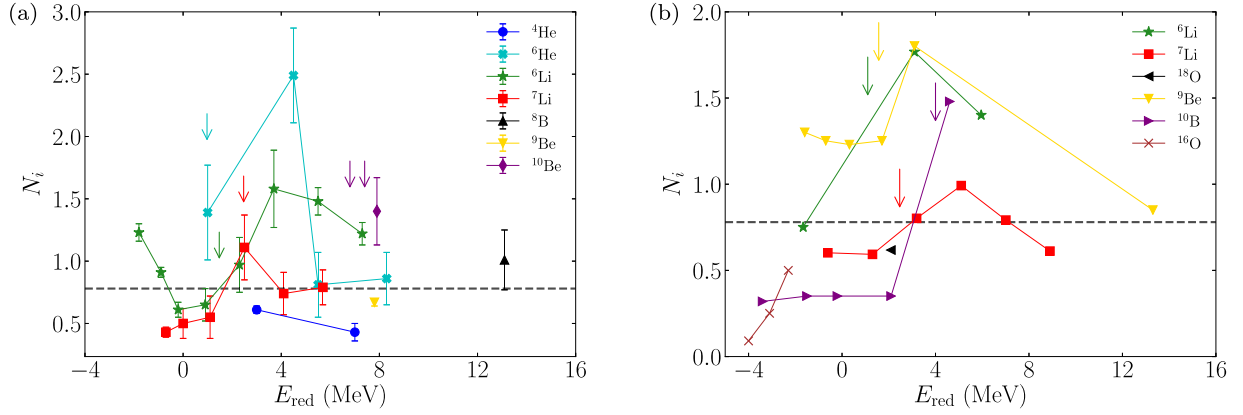


FIG. 14. N_i values, obtained from OM3, as a function of the reduced energy ($E_{\text{red}} = E_{\text{CM}} - V_B$), for several projectiles reacting on two different targets, at energies around the respective Coulomb barriers. The dashed line corresponds to $N_i = 0.78$ (extracted from [25]). (a) ^{64}Zn target (this study). The arrows indicate the main breakup Q values for ^6He , ^6Li , ^7Li , and ^{10}Be . (b) ^{120}Sn target (from [26]). The arrows indicate the main breakup Q values for ^6Li , ^7Li , ^9Be , and ^{10}B .

standard $N_i = 0.78$ value assumed by OM2. Combining both figures [Figs. 14(a) and 14(b)], we obtain some important results:

- (i) Considering the behavior of the stable weakly bound and exotic nuclei, for which we have data at several energies, the figures indicate increasing N_i parameter values in the following order: ^{10}B , ^7Li , ^6Li , ^9Be , and ^6He . This order is related to the binding energy of these nuclei (presented as Q values in Table I). These nuclei present cluster structures and can be considered as combinations of neutrons, isotopes of hydrogen $^{1,2,3}\text{H}$ and/or helium $^{3,4}\text{He}$; their reaction dynamics depend strongly on their respective structure and binding energy. This fact is evidenced by experimental observations of their reaction channels (see, for example, [33,37,41,43,46,47]).
- (ii) The best OP N_i parameter within the determined uncertainties, as a function of the reduced energy, presents a pronounced peak at energies above the Coulomb barrier, with a correlation with the corresponding projectiles' breakup Q value (Table I). In Fig. 14, such Q values are indicated with an arrow. For ^6He , we observe a pronounced peak at reduced energies above the $\alpha + 2n$ breakup mode ($Q = -0.975$ MeV). For ^9Be , we observe a pronounced peak at reduced energies above the $\alpha + \alpha + n$ breakup mode ($Q = -1.665$ MeV). For ^6Li , such a pronounced peak is observed at reduced energies above the $\alpha + d$ breakup mode ($Q = -1.474$ MeV). For ^7Li , the absorption peak is observed at the reduced energies above the $\alpha + t$ breakup mode ($Q = -2.468$ MeV). In the case of ^{10}B , presented in Fig. 14(b), for the reduced energies below its $^6\text{Li} + \alpha$ breakup mode ($Q = -4.461$ MeV), we have very low flux absorption [26,48,49]. For the higher reduced energy (data extracted from [50]), above its $^6\text{Li} + \alpha$ breakup mode ($Q = -4.461$ MeV), we verify a complete change in the flux absorption strength and another peak structure can be identified.

- (iii) Comparing $^9,^{10}\text{Be}$, measured at the same bombarding energy $E_{\text{CM}} = 24.5$ MeV (approximately 8 MeV above the Coulomb barrier), we obtain $N_i = 0.67$ for ^9Be and $N_i = 1.41$ for ^{10}Be best fits. The explanation for ^{10}Be absorption being greater than for ^9Be [$\alpha + \alpha + n$ breakup mode ($Q = -1.665$ MeV)] should be related to the reduced bombarding energy being higher (just above) than the energy need for opening the $^9\text{Be} + n$ ($Q = -6.812$ MeV) and $^6\text{He} + ^4\text{He}$ ($Q = -7.409$ MeV) breakup channels. At around the same energy, the ^9Be breakup (and then absorption) is shown to decrease at energies much higher than the reduced bombarding energy (close to the $\alpha + \alpha + n$ breakup mode ($Q = -1.665$ MeV)). In this sense, Figs. 14(a) and 14(b) corroborate each other. In addition, we have a result for ^8B : similarly to ^9Be , at a higher reduced bombarding energy (≈ 13 MeV) its breakup mode seems to be not as pronounced as it could be expected at a reduced bombarding energy close to $^7\text{Be} + p$ breakup channel ($Q = -0.136$ MeV). In [37], the authors report on a total breakup cross section of the order of 20–25% of the total reaction cross section, suggesting a different behavior between the p -halo ^8B and n -halo nuclei.

Thus, according to OM3 analysis, the yield of weakly bound nuclei breakup presents an optimum/maximum value, at a specific (peak defined) bombarding energy, that can be closely estimated. OM3 is shown to correlate the OP imaginary strength with the Coulomb barrier (V_B) of the interacting system and the projectile breakup Q value (Q_{bu}). The OP imaginary strength rises sharply at scattering energies just above the Coulomb barrier. Such an optimum energy (E_b^{op}) could be approximately estimated by $E_b^{\text{op}} \approx V_B + |Q_{\text{bu}}|$, where E_b^{op} would be the optimum bombarding energy for breaking the projectile up, V_B is the Coulomb barrier of the system, and $|Q_{\text{bu}}|$ is the modulus of the projectile cluster breakup Q value. Therefore, based on OM3, when the projectile bombarding energy exceeds the Coulomb barrier of the interacting system by approximately the modulus of the

TABLE VI. Results from OM1 fits for the elastic scattering angular distributions of ${}^7\text{Li}$ on ${}^{80}\text{Se}$ ($V_B \approx 13.7$ MeV).

E_{CM} (MeV)	χ_{red}^2
12.9	4.42
13.3	4.17
13.8	5.31
14.3	3.89
14.7	5.96
15.6	26
16.6	23
17.5	8.4
18.4	13
21.2	18
23.9	9.6

projectile breakup Q value, then we appreciate a pronounced increase of the OP imaginary strength. This result is further corroborated by experimental spectra presented, for instance, in [33,35–37,42]. The yield of the projectile breakup/transfer fragments observed in the experimental spectra is mainly responsible for decreasing elastic scattering with respect to the Rutherford cross section and is responsible for the sharp increase of the OP main parameter related to elastic scattering flux absorption. Furthermore, it is worth mentioning that it occurs not for one specific projectile, but for all weakly bound nuclei projectile under study.

Considering the ${}^{64}\text{Zn}$ target, we were able to cover three objectives: (i) to corroborate the previous result obtained for ${}^{120}\text{Sn}$ [26]; (ii) to demonstrate the target independence of the OM analyses; and (iii) to demonstrate the OM analyses for weakly bound nuclei reactions as being systematic (independent of projectile and target).

It is worth mentioning, once more, that the OP imaginary term was, from the beginning, assumed in a phenomenological way, through data fits, and did not provide a formal theoretical justification for its form factor and energy dependence. Even so, with OM3 and only one free parameter, with the respective uncertainties (obtained from χ^2 analysis), we are able to account mostly for the absorption process, which reflects, as a function of the energy, a large variety of physical effects.

The different behaviors presented by exotic nuclei ${}^6\text{He}$ and mainly ${}^{11}\text{Be}$ reactions were well explained by the Coulomb dipole polarization (CDP) potential, which takes into account the long range effect of the dipole Coulomb interaction. It has been demonstrated that CDP increases the breakup probability of exotic nuclei such as ${}^6\text{He}$, ${}^{11}\text{Li}$, and ${}^{11}\text{Be}$ [27,29]. The exotic nuclei present an amplified (and long range) absorption process due to breakup, which, depending on the atomic number of the target, can be produced and even dominated by Coulomb polarization effects [27,29]. In particular, in [33], the data for the ${}^6\text{He} + {}^{64}\text{Zn}$ show that the transfer and breakup mechanisms account for almost 80% of the total reaction cross section. In [36], the data for ${}^{11}\text{Be} + {}^{64}\text{Zn}$ show the suppression of the Coulomb nuclear interference peak and the extracted total-reaction cross section for ${}^{11}\text{Be}$ to be more than double

TABLE VII. The same as for Table VI, obtained from OM2.

E_{CM} (MeV)	χ_{red}^2
12.9	4.57
13.3	6.27
13.8	1.44
14.3	4.16
14.7	3.12
15.6	3.50
16.6	6.90
17.5	1.94
18.4	1.42
21.2	1.37
23.9	1.44

compared to the ones induced by ${}^{9,10}\text{Be}$. Such an enhancement of the total reaction cross section is reported as mainly due to transfer/breakup processes.

A. A further test of consistency for OM3

As a test of consistency, we propose to apply the method to another specific case: ${}^7\text{Li} + {}^{80}\text{Se}$, at energies around the Coulomb barrier. We take experimental elastic scattering angular distributions reported in [51], at eleven bombarding energies: 12.9, 13.3, 13.8, 14.3, 14.7, 15.6, 16.6, 17.5, 18.4, 21.2, and 23.9 MeV, in the center-of-mass frame. The Coulomb barrier of this system is around 13.7 MeV (in the center-of-mass frame).

Tables VI, VII, VIII and IX present the respective OP best fit (χ_{red}^2) results. For OM3 and OM4, in which N_i and (N_r, N_i) are, respectively, allowed to vary, best fit OP parameter(s) are reported with the respective uncertainties. From Tables VI to IX, we are able to observe the improvement of data fits based on χ_{red}^2 results.

Figure 15 presents experimental elastic scattering angular distributions compared to theoretical calculations based on the best OM variants (OM3 and OM4).

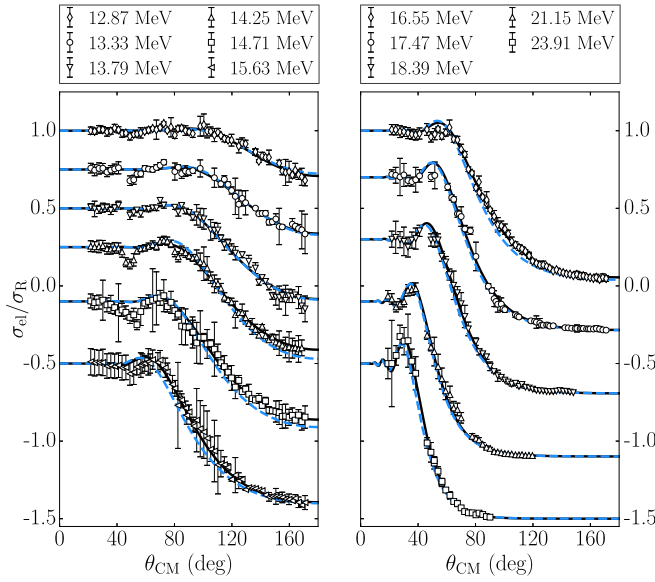
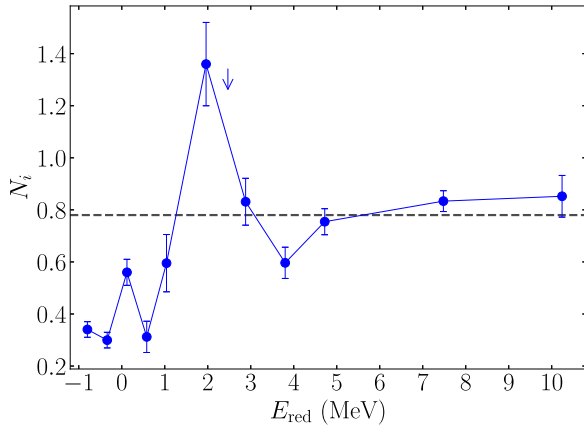
For comparison with Fig. 14, results of N_i as a function of the reduced energy, for the ${}^7\text{Li} + {}^{80}\text{Se}$ system, are presented in Table VIII and plotted in Fig. 16.

TABLE VIII. The same as for Table VI, obtained from OM3.

E_{CM} (MeV)	N_i	χ_{red}^2
12.9	0.34 ± 0.03	1.10
13.3	0.30 ± 0.03	1.03
13.8	0.56 ± 0.05	1.04
14.3	0.31 ± 0.06	2.50
14.7	0.60 ± 0.11	2.99
15.6	1.36 ± 0.16	2.39
16.6	0.83 ± 0.09	6.87
17.5	0.60 ± 0.06	1.57
18.4	0.75 ± 0.05	1.41
21.2	0.83 ± 0.04	1.31
23.9	0.85 ± 0.08	1.40

TABLE IX. The same as for Table VI, obtained from OM4.

E_{CM} (MeV)	N_r	N_i	χ_{red}^2
12.9	1.12 ± 0.06	0.25 ± 0.04	1.02
13.3	0.94 ± 0.06	0.40 ± 0.10	1.00
13.8	0.99 ± 0.03	0.58 ± 0.05	1.03
14.3	0.79 ± 0.03	0.56 ± 0.06	0.97
14.7	0.78 ± 0.03	0.66 ± 0.08	1.02
15.6	0.83 ± 0.02	0.78 ± 0.08	0.93
16.6	0.74 ± 0.02	0.74 ± 0.01	1.26
17.5	0.87 ± 0.03	0.51 ± 0.01	0.95
18.4	0.84 ± 0.03	0.52 ± 0.05	0.94
21.2	0.88 ± 0.06	0.68 ± 0.07	1.18
23.9	0.71 ± 0.05	0.42 ± 0.07	0.76


 FIG. 15. Experimental elastic scattering angular distributions for the ${}^7\text{Li} + {}^{80}\text{Se}$ reaction and corresponding OM3 (dashed blue) and OM4 (solid black) fits. Data were taken from [51].

 FIG. 16. OP imaginary strength represented by the N_i parameter (given by OM3), as a function of the reduced energy (E_{red}), for ${}^7\text{Li} + {}^{80}\text{Se}$, at energies around the Coulomb barrier. The solid line is a guide for the eyes. The dashed line corresponds to $N_i = 0.78$ (given by OM2). The arrow, as for Fig. 14, indicates the main breakup Q value of ${}^7\text{Li}$.

Considering OM3, at energies around the Coulomb barrier (V_B), the OP imaginary strength is shown to be relatively low. At energies around what we call the optimum bombarding energy (E_b^{op}), pointed out with an arrow on Fig. 16, we have a pronounced peak in the OM3 best fit N_i parameter. The same behavior was previously observed in Fig. 14 for ${}^{64}\text{Zn}$ and ${}^{120}\text{Sn}$, used as targets.

B. An alternative optical model (OM4)

OM4, based on Eq. (4), allowing both (N_r and N_i) parameters to vary, presents the best data fits (see Tables V and IX). The relaxation of the N_r phenomenological parameter, in this SPP OM variant, can compensate specific nuclear structure and dynamic effects, for instance nuclear densities variations and polarization processes. For the latter, the breakup threshold anomaly (BTA) [20–24,44,45] was reported for weakly bound nuclear reactions. The breakup process can produce a repulsive polarization potential that compensates the attractive potential produced by other direct reaction processes. Such an effect can be simulated by OM4 with OP real and imaginary renormalizations.

Using Figs. 8–12 and Table V, we can draw some conclusions. For OM4 most χ_{red}^2 results are around unity. Results for ${}^6\text{He}$ and ${}^{6,7}\text{Li}$ present an important reduction of the OP real strength, while the OP imaginary strength is high for ${}^6\text{He}$ and ${}^6\text{Li}$ around and just above the Coulomb barrier, reducing gradually with increasing energy. For ${}^7\text{Li}$, OP real and imaginary strengths results are quite similar, both below the unity, and a factor 2 less intense than ${}^6\text{Li}$, besides being much more constant (varying slightly) as a function of energy.

These results show some similarities with previous works. For instance, in [52], ${}^6\text{He} + {}^{208}\text{Pb}$ breakup cross sections were measured at 14, 16, 18, and 22 MeV (laboratory frame), with the Coulomb barrier of 18 MeV. The highest breakup differential cross section showed up at $V_B = 18$ MeV and decreased both at lower and higher energies with respect to V_B . In [53], ${}^{6,7}\text{Li} + {}^{138}\text{Ba}$ reaction cross sections were reported, at bombarding energies between 21 and 32 MeV, with $V_B \approx 23$ MeV. The reaction cross sections were shown to be similar at higher energies, and higher for ${}^6\text{Li}$ compared to ${}^7\text{Li}$ at lower energies (around the Coulomb barrier). These results are in agreement with OM4 applied to ${}^6\text{He}$ and ${}^6\text{Li}$. In [45], results obtained for the ${}^{6,7}\text{Li} + {}^{144}\text{Sm}$ systems showed that the OP imaginary potential does not vanish at the Coulomb barrier. For ${}^7\text{Li}$, OP real and imaginary strengths vary slightly with energy. The same behavior is observed, for instance, in Tables V and IX.

In any case, according to the literature [20,23,44,45], considering the same projectile ${}^6\text{Li}$ impinging on different targets, the behavior of OP real and imaginary strengths could depend on the target and system and/or the OP form factor.

For comparisons, we have inspected four cases: (1) ${}^{28}\text{Si}$ [44], (2) ${}^{116}\text{Sn}$ [23], (3) ${}^{144}\text{Sm}$ [45], and (4) ${}^{208}\text{Pb}$ [20]; (1) and (3) show one trend, the OP real strength increases and the imaginary strength decreases around and below the Coulomb barrier, while (2) and (4) show another trend: the OP real strength decreases and the imaginary strength increases around and below the Coulomb barrier. The former trend

does not agree with our (OM3 and OM4) results. The latter trend agrees with our (OM3 and OM4) analysis (see Tables V and IX).

Therefore, further studies must be developed to understand N_r and N_i variations, considering the respective uncertainties. Systematic analyses are already underway. New methods for uncertainty quantification in reaction theory [54–57] could be of value in future analyses.

Thus, OM4 should present some important advantages: it can (i) provide realistic OP for more complex reactions calculations, (ii) provide a better understanding of OP real and imaginary strengths and their dependence on energy, (iii) be a tool to revisit and shed light on BTA analyses, and (iv) favor the application of new methods of uncertainties quantification on BTA analyses (which were not in the scope of the current work).

V. SUMMARY AND CONCLUSIONS

We analyzed experimental elastic scattering angular distributions of ^4He , ^6Li , $^9,^{10,11}\text{Be}$, and ^8B impinging on the same (^{64}Zn) target, at bombarding energies around the respective Coulomb barriers.

Within the data set, we report on phenomenological OM calculations and the determined OP, based on the double-folding (DF) São Paulo potential (SPP) approach.

Within SPP, we report on four OM variants named OM1, OM2, OM3, and OM4.

OM1, with a different form factor, given by Eq. (2), takes into account internal fusion process and does not take into account strong surface absorption (SSA) processes. Thus, OM1 is range limited and fails when accounting for peripheral reaction channels.

OM2 accounts better for SSA however, it is also limited when applied to weakly bound nuclei reactions, at energies around the Coulomb barrier, where strong reaction (breakup) channels open and play an important role in the reactions dynamics.

As a systematic behavior observed in weakly bound reactions (derived mainly from SSA), the OP imaginary strength, necessary to fit experimental data, tends to vary with energy. It tends to be significant at lower energies (even below the Coulomb barrier) and increase with energy (around and above the Coulomb barrier). Such an increase is associated with open reaction channels, mainly the projectile breakup.

Thus, OM3 allows for OP imaginary strength to vary and, therefore, better (in terms of χ_{red}^2 and compared to OM1 and OM2) accounts for the loss of flux due to significant open reaction channels. Within OM3, such an increase is verified through the variation of the OP imaginary strength (N_i) parameter with energy. It rises sharply at scattering energies above the Coulomb barrier. The OM3 best fit (N_i) parameter correlates with projectile breakup Q value. Based on OM3 and the variation on the N_i parameter, an optimum bombarding energy for which the projectile breakup yield should be most favored can be approximately estimated, as a function of the Coulomb barrier of the interacting system and the projectile breakup Q value. It is shown to be systematical, when applying OM3 to the different weakly bound nuclei projectiles impinging on targets with different masses (and atomic numbers).

As a further independent test of consistency and generalization, we applied OM1 to OM4 to another specific case: $^7\text{Li} + ^{80}\text{Se}$. In Tables VI to IX, we are able to observe the improvement of data fits based on χ_{red}^2 results. OM3 and OM4 present much better results than OM1 and OM2.

Comparing OM3 and OM4, OM3 predicts a pronounced OP imaginary strength as a function of energy, while OM4 predicts a continuous high OP imaginary strength as a function of energy. The latter has a tendency of decreasing OP real strength mainly at energies around the Coulomb barrier. Results of both OM3 and OM4 seem to be correlated to the breakup of weakly bound nuclei.

Unlike OM3, OM4 allows also for OP real strengths to vary and presents the best data fits, with χ_{red}^2 results around unity for most of the data set. Such a parameter variation is justified by the breakup process, which can produce a repulsive polarization potential that compensates the attractive potential produced by other direct processes.

In particular, unlike ^7Li , with its first excited state at $E^* = 477.612(3)$ keV, the breakups of ^6Li and ^9Be , have their respective dissociation energies (Table I) smaller than their respective first excited states [$E^* = 2186(2)$ keV and $E^* = 1684(20)$ keV] [30]. Thus, breakup can result in a stronger and dominant direct reaction channel, besides leading to weak coupling between the elastic and other inelastic or transfer channels. It would mostly imply the need to renormalize OP real and imaginary strengths according to OM4. Thus, the OM4 variant, with OP fixed form factor represents a powerful tool to revisit and shed light on breakup threshold anomaly (BTA) analyses previously carried out for these nuclei.

Last but not least, these OM analyses tend to be range limited when analyzing exotic nuclei reactions, according to extensive studies reported in [27,29] (which were not in the scope of the current work). This effect has been shown to be more accentuated for exotic nuclei collisions with heavier targets, which tend to be insensitive to OM short range terms. Thus, for exotic nuclei, OM may need to include OP terms with longer ranges than the ones provided by OM1 to OM4 [27,29]. Using a ^{64}Zn target, exotic nuclei (^6He and ^{11}Be) were also analyzed, within the same OM frame, as reference and comparison points.

Therefore, our main conclusions are focused mainly on weakly bound nuclei reactions, at energies around the Coulomb barrier, within OM3 and OM4 analyses.

Within OM3 and OM4, further investigations would be of value for better mapping the OP strengths as a function of energy for weakly bound nuclei reactions, at energies around the Coulomb barrier. This will be pursued from now on.

ACKNOWLEDGMENTS

This work was developed within the context of the International Research Network for Nuclear Astrophysics (IReNA) and the Ibero-American Network of Nuclear Astrophysics (IANNA). The authors, as members of both networks, acknowledge all support and collaboration from IReNA and IANNA (National Science Foundation under Grant No. OISE-1927130).

- [1] H. Feshbach, C. E. Porter, and V. F. Weisskopf, *Phys. Rev.* **96**, 448 (1954).
- [2] H. Feshbach, *Ann. Phys. (NY)* **5**, 357 (1958).
- [3] G. R. Satchler, *Introduction to Nuclear Reactions* (Macmillan, New York, 1980),
- [4] G. Satchler and W. Love, *Phys. Rep.* **55**, 183 (1979).
- [5] J. Cook, *Nucl. Phys. A* **388**, 153 (1982).
- [6] D. T. Khoa, G. R. Satchler, and W. von Oertzen, *Phys. Rev. C* **51**, 2069 (1995).
- [7] R. Varner, W. Thompson, T. McAbee, E. Ludwig, and T. Clegg, *Phys. Rep.* **201**, 57 (1991).
- [8] M. Brandan and G. Satchler, *Phys. Rep.* **285**, 143 (1997).
- [9] D. T. Khoa and G. Satchler, *Nucl. Phys. A* **668**, 3 (2000).
- [10] C. Hebborn, F. M. Nunes, G. Potel, W. H. Dickhoff, J. W. Holt, M. C. Atkinson, R. B. Baker, C. Barbieri, G. Blanchon, M. Burrows, R. Capote, P. Danielewicz, M. Dupuis, C. Elster, J. E. Escher, L. Hlophe, A. Idini, H. Jayatissa, B. P. Kay, K. Kravvaris *et al.*, *J. Phys. G: Nucl. Part. Phys.* **50**, 060501 (2023).
- [11] M. A. Cândido Ribeiro, L. C. Chamon, D. Pereira, M. S. Hussein, and D. Galetti, *Phys. Rev. Lett.* **78**, 3270 (1997).
- [12] L. C. Chamon, D. Pereira, M. S. Hussein, M. A. Cândido Ribeiro, and D. Galetti, *Phys. Rev. Lett.* **79**, 5218 (1997).
- [13] L. C. Chamon, D. Pereira, and M. S. Hussein, *Phys. Rev. C* **58**, 576 (1998).
- [14] D. Galetti, S. S. Mizrahi, L. C. Chamon, D. Pereira, M. S. Hussein, and M. A. Cândido Ribeiro, *Phys. Rev. C* **58**, 1627 (1998).
- [15] L. C. Chamon, B. V. Carlson, L. R. Gasques, D. Pereira, C. De Conti, M. A. G. Alvarez, M. S. Hussein, M. A. Cândido Ribeiro, E. S. Rossi, and C. P. Silva, *Phys. Rev. C* **66**, 014610 (2002).
- [16] M. A. G. Alvarez, N. Alamanos, L. C. Chamon, and M. S. Hussein, *Nucl. Phys. A* **753**, 83 (2005).
- [17] G. Satchler, *Phys. Rep.* **199**, 147 (1991).
- [18] G. Satchler and W. Love, *Phys. Lett. B* **76**, 23 (1978).
- [19] G. Satchler, *Phys. Lett. B* **83**, 284 (1979).
- [20] M. S. Hussein, P. R. S. Gomes, J. Lubian, and L. C. Chamon, *Phys. Rev. C* **73**, 044610 (2006).
- [21] J. O. Fernández Niello, J. M. Figueira, D. Abriola, A. Arazi, O. A. Capurro, G. V. Martí, D. Martínez Heinmann, A. J. Pacheco, E. de Barbará, I. Padrón, P. R. S. Gomes, and J. Lubian, *Nucl. Phys. A* **787**, 484 (2007).
- [22] M. Zadro, P. Figuera, A. Di Pietro, F. Amorini, M. Fischella, O. Goryunov, M. Lattuada, C. Maiolino, A. Musumarra, V. Ostashko, M. Papa, M. G. Pellegriti, F. Rizzo, D. Santonocito, V. Scuderi, and D. Torresi, *Phys. Rev. C* **80**, 064610 (2009).
- [23] N. N. Deshmukh, S. Mukherjee, D. Patel, N. L. Singh, P. K. Rath, B. K. Nayak, D. C. Biswas, S. Santra, E. T. Mirgule, L. S. Danu, Y. K. Gupta, A. Saxena, R. K. Choudhury, R. Kumar, J. Lubian, C. C. Lopes, E. N. Cardozo, and P. R. S. Gomes, *Phys. Rev. C* **83**, 024607 (2011).
- [24] F. Gollan, D. Abriola, A. Arazi, O. Capurro, M. Cardona, E. de Barbará, D. Hojman, G. Martí, A. Pacheco, D. Rodrigues, and J. Testoni, *Nucl. Phys. A* **979**, 87 (2018).
- [25] M. A. G. Alvarez, L. C. Chamon, M. S. Hussein, D. Pereira, L. R. Gasques, E. S. Rossi, and C. P. Silva, *Nucl. Phys. A* **723**, 93 (2003).
- [26] M. A. G. Alvarez, J. P. Fernández-García, J. L. León-García, M. Rodríguez-Gallardo, L. R. Gasques, L. C. Chamon, V. A. B. Zagatto, A. Lépine-Szilý, J. R. B. Oliveira, V. Scarduelli, B. V. Carlson, J. Casal, A. Arazi, D. A. Torres, and F. Ramirez, *Phys. Rev. C* **100**, 064602 (2019).
- [27] M. A. G. Alvarez, M. Rodríguez-Gallardo, J. P. Fernández-García, J. Casal, and J. A. Lay, *Phys. Rev. C* **103**, 054614 (2021).
- [28] J. Fernández-García, M. Rodríguez-Gallardo, M. Alvarez, and A. Moro, *Nucl. Phys. A* **840**, 19 (2010).
- [29] J. P. Fernández-García, M. A. G. Alvarez, and L. C. Chamon, *Phys. Rev. C* **92**, 014604 (2015).
- [30] National Nuclear Data Center, NuDat database, www.nndc.bnl.gov/nudat3/.
- [31] L. Chamon, B. Carlson, and L. Gasques, *Comput. Phys. Commun.* **267**, 108061 (2021).
- [32] A. Di Pietro, P. Figuera, F. Amorini, C. Angulo, G. Cardella, S. Cherubini, T. Davinson, D. Leanza, J. Lu, H. Mahmud, M. Milin, A. Musumarra, A. Ninane, M. Papa, M. G. Pellegriti, R. Raabe, F. Rizzo, C. Ruiz, A. C. Shotter, N. Soic, and S. Tudisco, *Europhys. Lett.* **64**, 309 (2003).
- [33] A. Di Pietro, P. Figuera, F. Amorini, C. Angulo, G. Cardella, S. Cherubini, T. Davinson, D. Leanza, J. Lu, H. Mahmud, M. Milin, A. Musumarra, A. Ninane, M. Papa, M. G. Pellegriti, R. Raabe, F. Rizzo, C. Ruiz, A. C. Shotter, N. Soić, S. Tudisco, and L. Weissman, *Phys. Rev. C* **69**, 044613 (2004).
- [34] J. P. Fernández-García, A. Di Pietro, P. Figuera, J. Gómez-Camacho, M. Lattuada, J. Lei, A. M. Moro, M. Rodríguez-Gallardo, and V. Scuderi, *Phys. Rev. C* **99**, 054605 (2019).
- [35] M. Zadro, P. Figuera, A. Di Pietro, M. Fischella, M. Lattuada, T. Lönnroth, M. Milin, V. Ostashko, M. G. Pellegriti, V. Scuderi, D. Stanko, E. Strano, and D. Torresi, *Phys. Rev. C* **87**, 054606 (2013).
- [36] A. Di Pietro, G. Randisi, V. Scuderi, L. Acosta, F. Amorini, M. J. G. Borge, P. Figuera, M. Fischella, L. M. Fraile, J. Gomez-Camacho, H. Jeppesen, M. Lattuada, I. Martel, M. Milin, A. Musumarra, M. Papa, M. G. Pellegriti, F. Perez-Bernal, R. Raabe, F. Rizzo *et al.*, *Phys. Rev. Lett.* **105**, 022701 (2010).
- [37] R. Spartà, A. Di Pietro, P. Figuera, O. Tengblad, A. Moro, I. Martel, J. Fernández-García, J. Lei, L. Acosta, M. Borge, G. Bruni, J. Cederkäll, T. Davinson, J. Ovejas, L. Fraile, D. Galaviz, J. Halkjaer Jensen, B. Jonson, M. La Cognata, A. Perea, A. Sánchez-Benítez, N. Soić, and S. Viñals, *Phys. Lett. B* **820**, 136477 (2021).
- [38] I. J. Thompson, *Comput. Phys. Rep.* **7**, 167 (1988).
- [39] H. De Vries, C. De Jager, and C. De Vries, *At. Data Nucl. Data Tables* **36**, 495 (1987).
- [40] B. V. Carlson and D. Hirata, *Phys. Rev. C* **62**, 054310 (2000).
- [41] V. A. B. Zagatto, J. Lubian, L. R. Gasques, M. A. G. Alvarez, L. C. Chamon, J. R. B. Oliveira, J. A. Alcántara-Núñez, N. H. Medina, V. Scarduelli, A. Freitas, I. Padron, E. S. Rossi, and J. M. B. Shorto, *Phys. Rev. C* **95**, 064614 (2017).
- [42] J. P. Fernández-García, M. Zadro, A. Di Pietro, P. Figuera, M. Fischella, O. Goryunov, M. Lattuada, C. Marchetta, A. M. Moro, A. Musumarra, V. Ostashko, M. G. Pellegriti, V. Scuderi, E. Strano, and D. Torresi, *Phys. Rev. C* **92**, 054602 (2015).
- [43] A. Di Pietro, V. Scuderi, A. M. Moro, L. Acosta, F. Amorini, M. J. G. Borge, P. Figuera, M. Fischella, L. M. Fraile, J. Gomez-Camacho, H. Jeppesen, M. Lattuada, I. Martel, M. Milin, A. Musumarra, M. Papa, M. G. Pellegriti, F. Perez-Bernal, R. Raabe, G. Randisi *et al.*, *Phys. Rev. C* **85**, 054607 (2012).
- [44] A. Gómez Camacho, P. R. S. Gomes, and J. Lubian, *Phys. Rev. C* **82**, 067601 (2010).

- [45] J. M. Figueira, J. O. Fernandez Niello, A. Arazi, O. A. Capurro, P. Carnelli, L. Fimiani, G. V. Martí, D. Martinez Heimann, A. E. Negri, A. J. Pacheco, J. Lubian, D. S. Monteiro, and P. R. S. Gomes, *Phys. Rev. C* **81**, 024613 (2010).
- [46] A. Kundu, S. Santra, A. Pal, D. Chattopadhyay, R. Tripathi, B. J. Roy, T. N. Nag, B. K. Nayak, A. Saxena, and S. Kailas, *Phys. Rev. C* **95**, 034615 (2017).
- [47] N. Yu, H. Q. Zhang, H. M. Jia, S. T. Zhang, M. Ruan, F. Yang, Z. D. Wu, X. X. Xu, and C. L. Bai, *J. Phys. G: Nucl. Part. Phys.* **37**, 075108 (2010).
- [48] L. R. Gasques, A. S. Freitas, L. C. Chamon, J. R. B. Oliveira, N. H. Medina, V. Scarduelli, E. S. Rossi, M. A. G. Alvarez, V. A. B. Zagatto, J. Lubian, G. P. A. Nobre, I. Padron, and B. V. Carlson, *Phys. Rev. C* **97**, 034629 (2018).
- [49] M. A. G. Alvarez, M. Rodríguez-Gallardo, L. R. Gasques, L. C. Chamon, J. R. B. Oliveira, V. Scarduelli, A. S. Freitas, E. S. Rossi, V. A. B. Zagatto, J. Rangel, J. Lubian, and I. Padron, *Phys. Rev. C* **98**, 024621 (2018).
- [50] L. R. Gasques, M. A. G. Alvarez, A. Arazi, B. V. Carlson, L. C. Chamon, J. P. Fernández-García, A. Lépine-Szily, J. Lubian, J. Rangel, M. Rodríguez-Gallardo, V. Scarduelli, and V. A. B. Zagatto, *Phys. Rev. C* **103**, 034616 (2021).
- [51] L. Fimiani, J. M. Figueira, G. V. Martí, J. E. Testoni, A. J. Pacheco, W. H. Z. Cárdenas, A. Arazi, O. A. Capurro, M. A. Cardona, P. Carnelli, E. de Barbará, D. Hojman, D. Martinez Heimann, and A. E. Negri, *Phys. Rev. C* **86**, 044607 (2012).
- [52] D. Escrig, A. Sánchez-Benítez, A. Moro, M. A. G. Alvarez, M. Andrés, C. Angulo, M. Borge, J. Cabrera, S. Cherubini, P. Demaret, J. Espino, P. Figuera, M. Freer, J. García-Ramos, J. Gómez-Camacho, M. Gulino, O. Kakuee, I. Martel, C. Metelko, F. Pérez-Bernal, J. Rahighi, K. Rusek, D. Smirnov, O. Tengblad, and V. Ziman, *Nucl. Phys. A* **792**, 2 (2007).
- [53] A. M. M. Maciel, P. R. S. Gomes, J. Lubian, R. M. Anjos, R. Cabezas, G. M. Santos, C. Muri, S. B. Moraes, R. L. Neto, N. Added, N. C. Filho, and C. Tenreiro, *Phys. Rev. C* **59**, 2103 (1999).
- [54] A. J. Koning, *Eur. Phys. J. A* **51**, 184 (2015).
- [55] G. Schnabel, H. Sjöstrand, J. Hansson, D. Rochman, A. Koning, and R. Capote, *Nucl. Data Sheets* **173**, 239 (2021).
- [56] A. E. Lovell, F. M. Nunes, M. Catacora-Rios, and G. B. King, *J. Phys. G: Nucl. Part. Phys.* **48**, 014001 (2021).
- [57] C. D. Pruitt, J. E. Escher, and R. Rahman, *Phys. Rev. C* **107**, 014602 (2023).